Materials Horizons

ROYAL SOCIETY OF CHEMISTRY

COMMUNICATION

View Article Online
View Journal

Cite this: DOI: 10.1039/d5mh01199j

Received 23rd June 2025,
Accepted 7th August 2025

DOI: 10.1039/d5mh01199j

rsc.li/materials-horizons

Unlocking triple-band persistent luminescence: invisible UVC–UVB and visible red emission through structural modulation of $Na_2SrSi_2O_6:Pr^{3+}$ cyclosilicate

Yi Wang,[a] Jiaren Du, *[a] Hengwei Lin, [a] Dirk Poelman [b] and Eugeniusz Zych[c]

Materials that emit ultraviolet C (UVC) or ultraviolet B (UVB) radiation are essential in domains such as environmental surveillance, public health, and optoelectronic technologies, owing to their elevated photon energy and distinct optical characteristics. However, the development of innovative persistent luminescent phosphors exhibiting emission within the UVC or UVB spectral range continues to pose a considerable challenge. Herein we present a novel Pr^{3+}-doped $Na_2SrSi_2O_6$ phosphor featuring a cyclosilicate framework, which exhibits sustained photon emission in the UVC and UVB regions, alongside luminescence in the red spectral range. The $Na_2SrSi_2O_6:Pr^{3+}$ phosphor demonstrates pronounced and long-lasting UVC, UVB and red persistent luminescence following X-ray excitation, underscoring its effectiveness for utilization in both dark and bright environments. Moreover, the incorporation of smaller ionic radius co-dopants such as Mg^{2+} or Ca^{2+} effectively enhances the red emission intensity of the phosphor. In contrast, the introduction of the larger ionic radius co-dopant Ba^{2+} not only enhances the content of UVC emission but also improves the overall luminescent efficacy. As the content of Ba^{2+} increases, the phosphor exhibits a spectral transition from UVC to UVB within the ultraviolet region. Notably, the applications of this phosphor were assessed in bright-field and dark-field imaging, showcasing its considerable potential for high-contrast monitoring in bright daylight, and advanced optical marking technologies. This work advances the development of visible-to-invisible persistent luminescent materials and offers a good example of engineering the cyclosilicate matrices for luminescence spectrum tuning.

New concepts

Materials that emit ultraviolet-C (UVC), or ultraviolet-B (UVB) radiation are pivotal in fields such as environmental monitoring, public health, and optoelectronic technologies, due to their high photon energy and unique optical properties. However, current strategy to make a persistent luminescent phosphor emitting within the UVC or UVB spectral regions remains a big challenge. In this study, we present the unprecedented triple-band persistent luminescence spanning the UVC, UVB, and visible red spectral regions through engineering of $Na_2SrSi_2O_6$ cyclosilicate matrices. The incorporation of smaller ionic radius ions markedly enhances the intensity of red emission. In contrast, the addition of larger ionic radius ions not only elevates the UVC emission output but also boosts the overall luminescent efficiency. Moreover, with an increasing content of Ba^{2+}, the phosphor exhibits a luminescent transition from UVC to UVB within the ultraviolet spectrum. The performance was assessed in both bright-field and dark-field imaging applications, indicating promising prospects for advanced optical marking technologies.

1. Introduction

Persistent luminescence (PersL) is a unique optical phenomenon in which a phosphor continues to give light emission for a long period (seconds, minutes, or even hours) after stopping the external excitation source. Persistent phosphors in visible and near-infrared spectral ranges have been extensively investigated over the past decade, both in the scientific community and industry.[1–5] The combination of transition metals (Cr^{3+}, Mn^{2+}, Mn^{4+}, Mn^{5+}, Fe^{3+}, Ni^{2+}) or rare earth metals (Eu^{2+}, Ce^{3+}, Eu^{3+}, Dy^{3+}, Tb^{3+}, Sm^{3+}, Pr^{3+}) with a variety of host matrices of different crystal structures (perovskite, double perovskite, garnet, spinel) has provided a well-established and abundant platform for a carefully chosen visible-to-near-infrared emitting persistent phosphor in demand.[6–13]

Unlike visible photons, high-photon energy of ultraviolet (UV) radiation offers unique advantages in a wide field of view, such as invisible imaging markers in bright environments and sterilization.[14–16] PersL at the high-energy spectral domain (ultraviolet C, UVC, and ultraviolet B, UVB) plays an irreplaceable role in medical disinfection, photodynamic therapy, photocatalysis, daylight glowing tags and X-ray dosimetry.[17–19] For example, UVB, ranging from 280 to 315 nm, exhibits unique effectiveness against skin disorders and diseases such as

[a] International Joint Research Center for Photo-responsive Molecules and Materials, School of Chemical and Material Engineering, Jiangnan University, 214122 Wuxi, China. E-mail: jiaren.du@jiangnan.edu.cn
[b] LumiLab, Department of Solid State Sciences, Ghent University, Krijgslaan 281-S1, Ghent B-9000, Belgium
[c] Faculty of Chemistry, University of Wroclaw, 14. F. Joliot-Curie Street, 50-383 Wroclaw, Poland

vitiligo, eczema, and psoriasis. UVB is also gaining increasing attention in biomedicine for its role in promoting the synthesis of vitamin D in human bodies. UVC (covering the 200 and 280 nm range of wavelengths), as a component of sunlight, cannot reach the Earth surface due to the total absorption by the ozone layer. This makes UVC radiation vital in concealed communication, solar-blind optical tagging and high-contrast background-free imaging.[20,21] Both UVC and UVB radiations play important roles in many critical applications including printing, coatings, resins, labeling, dynamic tracking and anti-counterfeiting.[22–24] UVC photons facilitate efficient sterilization and high-level optical information storage functionalities.[25,26] The above-mentioned unconventional applications are beyond the expectations from traditional persistent phosphors giving visible light emission.[16,27]

However, the limited number of high-efficiency UVC and/or UVB persistent phosphors has become a drag on these promising applications. Moreover, rare-earth-based UV emitting materials are usually restricted to single-wavelength profiles, which hinders the exploration of new applications. UV phosphors capable of contributing also visible luminescence are expected to be a promising approach for multi-functionality which opens a broader range of possible novel and emerging applications. However, designing novel persistent phosphors with UVC–UVB dual bands or UVC–UVB-visible triple bands remains a challenge.[28,29] Difficulties in UVC–UVB material development are foreseeable and come from many aspects. For instance, seeking emission bands at different quite well spread wavelengths often implies an increase in the number of luminescent centers. This necessitates the use of co-doping strategies to introduce more luminescent ions, thereby increasing the complexity of material design and its synthesis. Additionally, both an appropriate matrix and an efficient emitting center are required. A matrix with a sufficiently broad bandgap (>5 eV if UVC emission is to be generated) and suitable crystal field environment is necessary to ensure the small Stokes shift to prevent thermal quenching and self-absorption of the emitted light. Moreover, the occurrence of UVC or UVB emissions relies on a preferable energy location of the excitation transitions, which is associated with principal composition, lattice structure, and crystal field control.[30] Furthermore, the number of intrinsic defects in the vicinity of the luminescent centers, the nature of traps and the probability of the charge carriers trapping–detrapping should be considered and managed for persistent luminescence to occur. There is a complex interplay and tradeoff among the selected matrix, trapping centers and emitters, which relates to the probability of radiative transitions in the desired UV range, nonradiative relaxation, or the presence of sharp-line intra-configurational transitions of lanthanide ions (typical $4f^n \rightarrow 4f^n$ transition).[18,31]

Pr^{3+}-activated UVC phosphors have been extensively studied before 2020[32–34] and several Pr^{3+}-activated UVC persistent phosphors and their daytime tracking capabilities were reported after 2020.[16,18,35,36] The advancement of Pr^{3+}-doped UVC PersL phosphors has accelerated significantly in recent years, leading to the emergence of a variety of materials. In the present work, a series of Pr^{3+}-doped cyclosilicate-based UVC–UVB-red triple-band persistent phosphors ($Na_2SrSi_2O_6:Pr^{3+}$) has been successfully synthesized. This phosphor exhibits intense UVC, UVB and red afterglow lasting over 30 minutes. Alongside thorough spectral analyses, trapping and detrapping processes have been comprehensively studied using a set of X-ray charging and thermoluminescence (TL) measurements to understand the underlying triple-band luminescence mechanisms. By manipulating the host composition *via* the partial substitution of Sr sites with Mg/Ca/Ba ions, triple-band PersL and emission variations are carefully investigated. The triple-band PersL covering both invisible and visible spectral regions offers new perspectives in the readout of encrypted optical information, bright-field surveillance, and tagging applications.

2. Results and discussion

The trigonal crystal structure of $Na_2SrSi_2O_6$ belongs to the $R\bar{3}m$ space group, characterized by lattice parameters of $a = b = 10.697$ Å, $c = 13.493$ Å, $\alpha = \beta = 90^\circ$, $\gamma = 120^\circ$ and a cell volume of $V = 1337.357$ Å^3.[37] This structure is classified as a cyclosilicate comprising hexameric rings $(Si_6O_{18})^{12-}$ arranged around an axis.[38,39] The connectivity among these rings is facilitated by four symmetry-independent M sites, occupied by sodium and/or strontium ions. The alkali and alkaline earth metal atoms are coordinated with six oxygen ligands, as illustrated in Fig. 1a. Due to the similarities in the valence state and the ionic radii of Pr^{3+} (0.99 Å, CN = 6) and Sr^{2+} (1.18 Å, CN = 6),[40] it is likely that the Pr^{3+} ion occupies the lattice position of Sr^{2+} in the $Na_2SrSi_2O_6$ structure rather than those of Na^+ (1.02 Å, CN = 6). Si^{4+} is, obviously, too small (0.26 Å, CN = 4) to be substituted by this dopant. The large charge mismatch possibly prevents or at least hinders substitution Na^+ with Pr^{3+}.

The phase purity and compositions of the synthesized phosphor were assessed using powder X-ray diffraction (XRD) measurements. The XRD pattern for $Na_2SrSi_2O_6$:1.5%Pr^{3+} is presented in Fig. 1b and is typical for other Pr concentrations. All observed diffraction peaks align with the standard $Na_2SrSi_2O_6$ phase (PDF no. 01-074-3938), confirming that incorporation of Pr^{3+} ions does not alter the phase of the $Na_2SrSi_2O_6$ host. To evaluate the morphology and homogeneity of the sample, scanning electron microscopy (SEM) images and energy-dispersive X-ray spectroscopy (EDS) elemental mapping of $Na_2SrSi_2O_6$:1.5%Pr^{3+} were obtained, as shown in Fig. 1c and d. The particles display non-uniform shapes, having diameters that vary between 1 and 5 μm. EDS elemental mapping identified signals for Sr, Si, O, and Na, as well as a less intense signal for Pr. These elements are evenly spread throughout the sample. The results are consistent with the anticipated chemical composition, and the uniform distribution of these elements indicates that the produced $Na_2SrSi_2O_6:Pr^{3+}$ phosphor is of a single cyclosilicate phase.

We subsequently explored the photoluminescent characteristics of the $Na_2SrSi_2O_6:Pr^{3+}$ phosphor. The Pr^{3+} ion possesses exceptionally unique and diverse energy levels, enabling

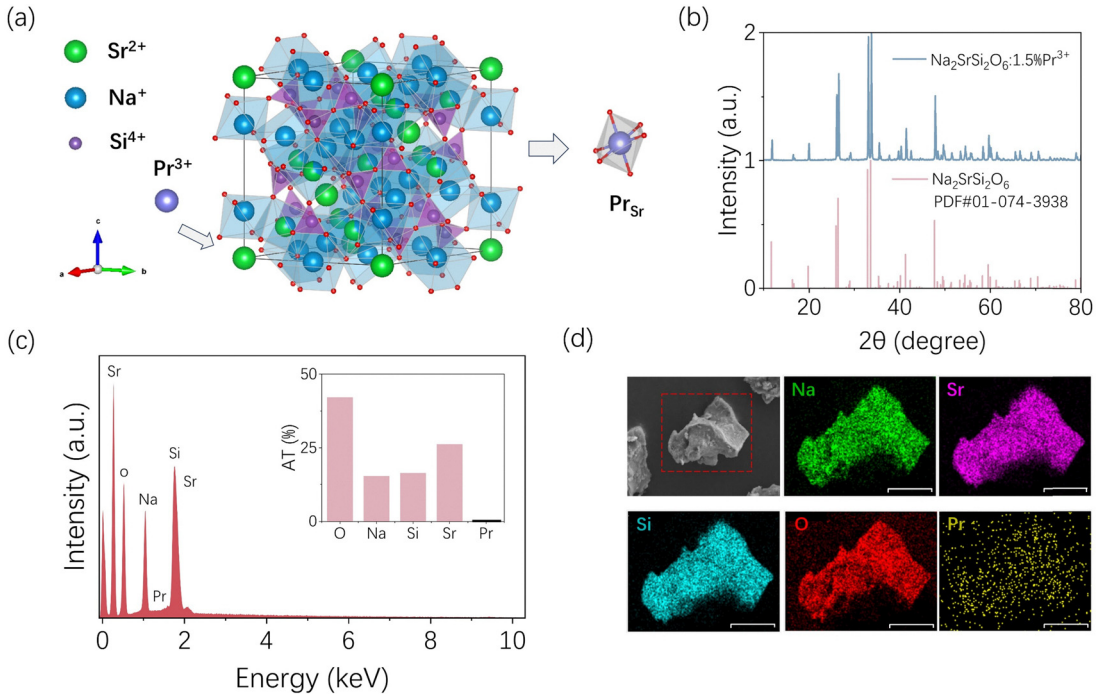

Fig. 1 (a) Crystal structure of $Na_2SrSi_2O_6$ and the occupation sites of Pr^{3+} ions; (b) XRD patterns of $Na_2SrSi_2O_6$:1.5%Pr^{3+} phosphors; (c) EDS spectrum of the material; (d) SEM and EDS mapping images of $Na_2SrSi_2O_6$:1.5%Pr^{3+} phosphor. A scale bar of 10 μm was used in EDS mappings.

it to generate a variety of luminescent features across ultraviolet, visible, and infrared radiation depending of host lattices. When excited by 245 nm UV irradiation, $Na_2SrSi_2O_6$:1.5%Pr^{3+} exhibits triple photoluminescence (PL) bands in the UVC, UVB, and red spectral regions, as illustrated in Fig. 2a. The emission peaks observed at 269 nm (UVC) and 310 nm (UVB) are attributed to the efficient inter-configurational transitions of Pr^{3+} ions from the lowest 4f5d state to the $^3H_{4,5,6}$, and $^3F_{2,3,4}$ levels, whereas the peak at 610 nm is due to transitions from the $^1D_2$ to the $^3H_4$ level.[16,41] The above assignment needs more explanation. In the red part of spectrum one can expect emission from $^1D_2$ overlapping with luminescence from $^3P_0$ to different Pr^{3+} levels, mainly to $^3H_6$ and $^3F_{2,3,4}$. Typically, for unambiguous assignment the lines in red one need to take advantage of time resolved emission spectroscopy (TRES), as emission from $^1D_2$, being both spin- and parity-forbidden lasts one or sometimes two orders of magnitude longer than luminescence from $^3P_0$, which are spin-allowed. In the case of $Na_2SrSi_2O_6$:Pr^{3+}, we may assume that the red luminescence related to $^3P_0$ level must be of very low intensity at most. This conclusion comes from the fact that the bluish-green luminescence around 480 nm, resulting from $^3P_0 \rightarrow {}^3H_4$ transition, is almost completely depleted. Consequently, also the transitions from this level in the red part have to be very weak. In such circumstances, the TRES experiments are not needed to state that the red luminescence of $Na_2SrSi_2O_6$:Pr^{3+} results from $^1D_2$ level of Pr^{3+} and possible contribution from $^3P_0$ is negligible. The photoluminescence excitation (PLE) spectrum monitoring the UVC emission at 269 nm is shown in Fig. S1.

Generally, Pr^{3+} displays two main types of luminescent transitions: the intra-configurational transitions from $4f^2$ to $4f^2$ and the inter-configurational transitions from 4f5d to $4f^2$, as demonstrated in Fig. 2b. The latter, being a fast-decaying emission, was often investigated for scintillation purposes upon excitation with X- or γ-rays. Notably, like some other phosphors, $Na_2SrSi_2O_6$:Pr^{3+} can be efficiently excited by standard ultraviolet light sources raising electrons from the $^3H_4$ ground level to $4f^15d^1$ state.[42,43] This results in intense 5d → 4f UVC luminescence and the less intense red emission from $^1D_2$, as already seen in Fig. 2a. Analyzing the published data for Ce-doped $Na_2SrSi_2O_6$, its bandgap is larger than 6 eV.[39] It is ideal for facilitating the electronic transitions of Pr^{3+} and prevents a low-temperature 5d → 4f luminescence quenching of the dopant, thus allowing for emissions in the visible light, UVB, and UVC ranges.

We also present the two-dimensional PLE and PL spectra of $Na_2SrSi_2O_6$:Pr^{3+} (Fig. 2c), demonstrating UVC and UVB emission across a range of excitation wavelengths. The XRD patterns for the synthesized $Na_2SrSi_2O_6$:x%Pr^{3+} samples (where x = 0.25, 0.5, 0.1, 0.15, 0.2) are also presented in Fig. S2a. All observed diffraction peaks correspond to the standard XRD patterns of the $Na_2SrSi_2O_6$ host (PDF no. 01-074-3938), indicating that the incorporation of the minor amount of Pr^{3+} ions does not alter the main phase of the $Na_2SrSi_2O_6$ matrix. The PL spectra for $Na_2SrSi_2O_6$:x%Pr^{3+} are presented in Fig. S2b, indicating that the intensity of the 5d → 4f emission bands grow up to 1.5% of Pr concentration and subsequently it declines. This may be taken as a rough estimation of the optimal concentration for PL, but not necessary for PersL.

Fig. 2d shows the steady-state radioluminescence of $Na_2SrSi_2O_6$:1.5%Pr^{3+} phosphor. Note that radioluminescence from

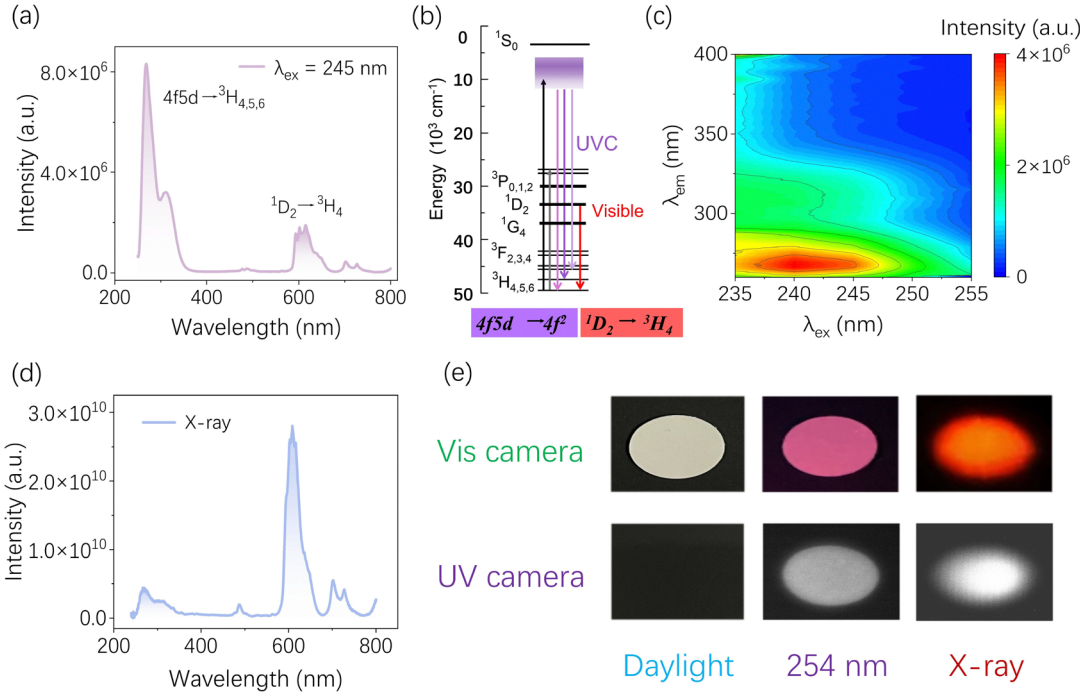

Fig. 2 (a) UV-Vis emission spectrum of $Na_2SrSi_2O_6:Pr^{3+}$ phosphor under 245 nm excitation; (b) energy levels diagram of the Pr^{3+} $4f^2$–4f5d configuration, showing possible excitation (upward arrow lines) and emission (downward arrow lines) transitions in the UV and visible light regions; (c) 2D PLE–PL plot of $Na_2SrSi_2O_6:Pr^{3+}$ phosphor in UV part of spectrum as a function of emission wavelength (λ_{em}) upon UV excitation with a variety of wavelengths (λ_{ex}); (d) X-ray excited UV-vis emission spectra of $Na_2SrSi_2O_6$:1.5%Pr^{3+} phosphor; (e) images of the samples taken with a regular visible light camera, exposed to daylight, 254 nm, and X-ray irradiation (top row), and images taken with a UV sensitive camera under the same conditions (bottom row).

$^3P_0$ at about 490 nm is seen only as a residue again. The spectrum encompasses a wide range of wavelengths with clearly seen (though less-intense than in PL) 5d → 4f in UVB and UVC and the strongest red emission related to the relaxation of the $^1D_2$ level of Pr^{3+} ions. Thus, X-rays populate the $^1D_2$ level more effectively than it happens upon optical excitation at 245 nm. We hypothesize that this phenomenon arises from the energy disparity of the excitation source. Generally, the transitions from 4f to 5d in Pr^{3+} usually follow selection rules, making such transitions more allowed (*i.e.*, having a higher transition probability). Conversely, f–f transitions (specifically, transitions from 4f to 4f states) are typically considered forbidden or exhibit diminished intensity due to their lower absorption cross-section. Upon ultraviolet excitation, while f–f transitions may present certain possibilities, the excitation to the 5d orbital typically occurs at a more rapid rate, resulting in heightened non-radiative energy dissipation, which consequently diminishes the observed intensity of f–f transitions. Conversely, the circumstances alter when subjected to high-energy X-ray irradiation. The energy associated with X-rays is significantly greater than that of ultraviolet radiation, leading to a more potent excitation capability that can effectively promote electrons to elevated energy states (for instance, beyond the 5d level). The excited electrons have a high probability of undergoing relaxation transitions to the $^1D_2$ level, facilitating the transition from $^1D_2$ to $^3H_4$, which in turn amplifies red light emission. Moreover, we postulate that X-ray irradiation may facilitate more intricate electronic transition mechanisms, incorporating the influences of lattice vibrations and the crystal field, thus amplifying the f–f transition phenomena.

We acquired images of the sample illuminated by daylight, 254 nm ultraviolet radiation, and upon exposure to X-rays utilizing a standard visible light camera as well as using a UV-sensitive camera, as illustrated in Fig. 2e. The much stronger orange luminescence upon X-rays compared to 254 nm excitation is proved by the images. It appears from the spectra and the images that the $Na_2SrSi_2O_6:Pr^{3+}$ phosphor shows potential for multimodal information readout and anti-counterfeiting applications.

After cessation of X-ray irradiation, the $Na_2SrSi_2O_6:Pr^{3+}$ phosphor exhibited long-lasting red and UVC–UVB emission. Fig. 3a shows the persistent luminescence decay curve of the $Na_2SrSi_2O_6:Pr^{3+}$ monitored at 608 nm after irradiation with varying doses of X-rays. The intensity of the red afterglow exhibited a rapid decline during the initial minutes, followed by a gradual, practically single exponential, decay that persisted until the end of the measurement period of 500 s. Remarkably, even at the termination of the experiment, the afterglow intensity was still approximately two orders of magnitude greater than the baseline, indicating a robust and enduring red afterglow. The decay curve of UVB persistent luminescence of $Na_2SrSi_2O_6$:1.5%Pr^{3+} phosphor monitored at 313 nm after X-ray irradiation is given in Fig. S3. It presents a non-exponential character. Furthermore, Fig. 3b presents the decay profile of UVC afterglow from the $Na_2SrSi_2O_6:Pr^{3+}$ phosphor, as monitored at 269 nm following varying doses of X-rays.

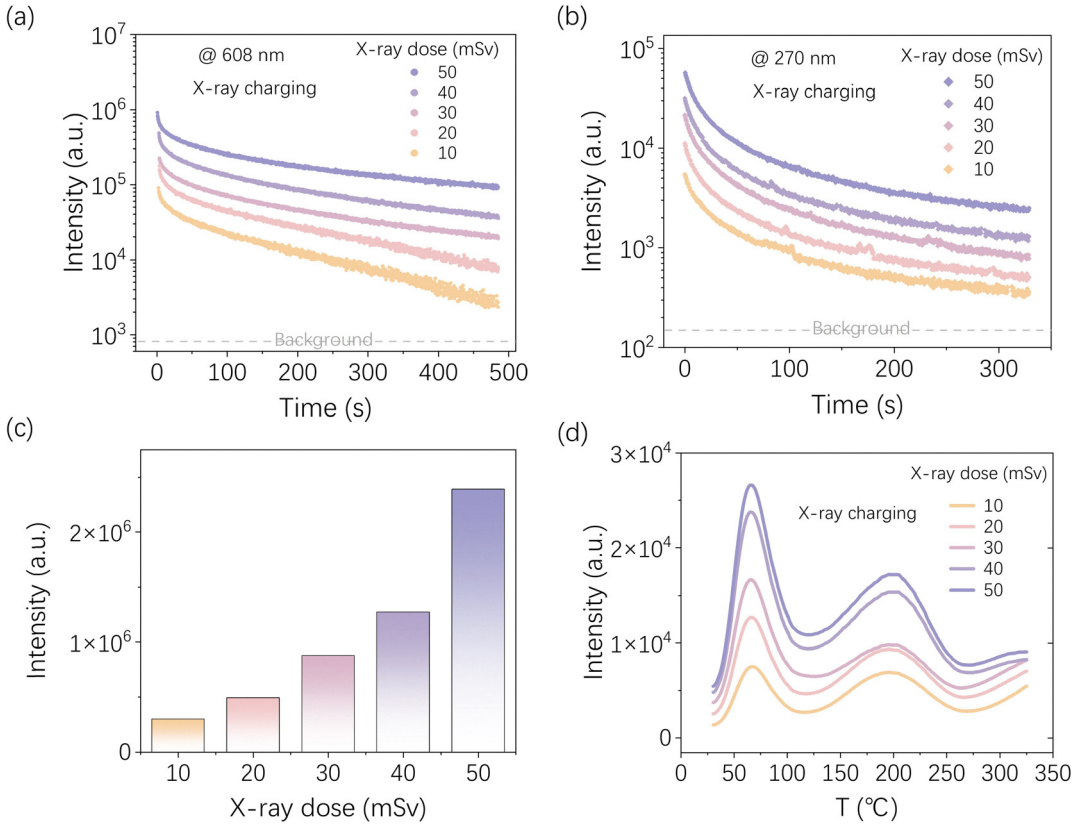

Fig. 3 Decay curves of persistent luminescence for $Na_2SrSi_2O_6$:1.5%Pr^{3+} phosphor monitored at 608 nm (a), or at 269 nm (b) after different does of X-rays; (c) analysis of the cumulative UVC persistent luminescence decay intensity as a function of X-ray dose, obtained through the integration of the persistent luminescence decay profile; (d) TL glow curves of $Na_2SrSi_2O_6$:1.5%Pr^{3+} phosphor after X-rays irradiations of varying doses.

The UVC afterglow demonstrated a pronounced intensity, remaining easily recordable even at a minimal X-ray exposure of 10 mSv, with the decay curve significantly surpassing the ambient background levels. Kinetic of the UVC afterglow is non-exponential.

Analysis of the cumulative persistent luminescence decay intensity as a function of X-ray dose (shown in Fig. 3c), was obtained through the integration of the UVC persistent luminescence decay profile (in Fig. 3b). It clearly shows that the system is not saturated after 50 mSv dose. These results were supplemented by thermoluminescence (TL) measurements to learn on the carrier traps characteristics, their depths and distribution. This is also an effective tool for assessing the storage capacity of persistent and storage phosphors.[44–46] Fig. 3d presents the TL glow curves of the $Na_2SrSi_2O_6$:Pr^{3+} phosphor, subjected to varying irradiation doses under dark conditions at ambient temperature.

This analysis provides insights into the distribution of energy traps in $Na_2SrSi_2O_6$:1.5%Pr^{3+}. Each TL glow curve consists of two prominent bands, with peaks located at approximately 66 °C and 194 °C. It is also observed that even with the exclusion of TL background signals, such as black-body radiation, the TL glow curve persists in ascending beyond 300 °C, suggesting the presence of additional, yet deeper, trap(s) in the system. With an increase in the X-ray dose, the low-temperature TL band (66 °C) peaks at the same temperature, whereas the high-temperature TL band (194 °C) progressively moves to higher temperatures though the shift is quite small and does not exceed 7–8 degrees. This observation suggests some interplay between different traps within this phosphor. The depths of the traps were estimated utilizing the modified trapping energy eqn (1):[47]

$$E = (-0.94 \ln \beta + 30.09) k T_m, \quad (1)$$

where k is the Boltzmann constant, with a value of 8.617×10^{-5} eV K^{-1}. E is the trap depth or activation energy, β is the constant heating rate, and T_m is the temperature of the TL peak.

The low-temperature trap depth is approximately 0.88 eV. At the dose of 10 mSv, the high-temperature trap depth measures 1.21 eV and it increases to 1.23 eV as the irradiation dose rises to 50 mSv. This trend suggests a continuous distribution of trap energies in the case of the TL around 195 °C in $Na_2SrSi_2O_6$:Pr^{3+} phosphor. Furthermore, we augmented the thermoluminescence spectra of the sample following a ten-minute exposure to X-ray irradiation, subsequently subjected to thermal treatment at 300 °C (in Fig. S4). However, due to detector limitations, detecting the UVC range poses challenges. Nevertheless, by combining the PL and afterglow decay curves, we can infer that the electrons captured during the X-ray

charging process can be released through their respective pathways (UV and visible emission). The TL results and the discussed kinetic data of PersL indicate that $Na_2SrSi_2O_6:Pr^{3+}$ can accommodate a substantial density of charge carriers and possesses commendable storage capability for long-lasting UVC, UVB and red persistent emissions. In contrast to traditional afterglow materials that are restricted to use in low-light or dark field conditions, the $Na_2SrSi_2O_6:Pr^{3+}$ phosphor offers significant advantages for high-precision optical marking applications across both bright and dark field environments, owing to its capacity for simultaneous emission of UVC, UVB, and red afterglow.

Fig. S5a and b display the survey XPS spectrum of the $Na_2SrSi_2O_6:Pr^{3+}$ phosphor and the high-resolution XPS spectrum with fitting analysis for the oxygen species, respectively. All constituents of the composition were accurately identified within the comprehensive XPS profile, as anticipated. Oxygen species fitting analysis shows that there are two distinct peaks at 531.0 eV and 531.9 eV, attributed to lattice oxygen and adsorbed oxygen, respectively.[48,49] It is noteworthy that the peak at 536 eV in the spectrum is attributed to the Auger peak of Na.[50] The high-resolution XPS spectra with their corresponding fitting curves for Sr 3d, Si 2p, and Na 1s are also presented in Fig. S6. Furthermore, electron paramagnetic resonance (EPR) spectroscopy confirmed the presence of oxygen vacancies (in Fig. S7) showing EPR signal at $g = 2.003$ originating from unpaired electrons in the oxygen vacancies only after exposure of the material to X-rays.[51] This signal was hardly recordable before irradiation with X-rays. This indicates that the trapping–detrapping process in $Na_2SrSi_2O_6:Pr^{3+}$ phosphor is associated with filling the O-vacancies with excited electrons. Since Pr^{3+} can easily get converted to Pr^{4+}, we may then formulate the trapping process with eqn (2) for hole trapping and eqn (3) for electron trapping using the standard Kröger–Vink notation of defects:

$$Pr_{Sr}^{\bullet} + h^{\bullet} \rightarrow Pr_{Sr}^{\bullet\bullet} \quad (2)$$

$$V_O^{\bullet\bullet} + e' \rightarrow V_O^{\bullet} \quad (3)$$

For phosphors exhibiting multiple emission bands, which is the case of $Na_2SrSi_2O_6:Pr^{3+}$, it is essential to learn how to manage the relationship among these emission features. Considering the competitive interaction among emission bands (UVC, UVB, and red portions), we considered it important to further examine the possibility of tuning their contributions by varying the composition of the host lattice.

The selection of Pr^{3+} transitions is likely to occur when the excited state of Pr^{3+} reaches the crossing point of two potential energy parabolas (the 4f5d state and the next lower-lying ^3P_J levels). If there is a large activation energy gap (ΔE) between the bottom of the excited state 4f5d and the crossing point, the phosphor will more likely undergo radiative transitions in the form of UV emission. Conversely, with the assistance of host phonons, the excited electron may non-radiatively relax to the $^3P_0$ state and then radiatively decay emitting visible light. Alternatively, it may further lose energy through $^3P_0$-to-$^1D_2$ multi-phonon relaxation, eventually producing red phonons *via* the $^1D_2 \rightarrow {}^3H_J$ transition.[42] Considering that the 4f5d energy level of Pr^{3+} is sensitive to the changes in the ion environment symmetry, we decided to replace some Sr with Mg, Ca, or Ba in the host lattice.

A series of solid solutions $Na_2Sr_{1-x}Mg_xSi_2O_6:Pr^{3+}$ and $Na_2Sr_{1-x}Ca_xSi_2O_6:Pr^{3+}$ were synthesized and Fig. S8 and S9 present their XRD patterns. When the value of x surpasses 0.2, a minor impurity phase emerges in these solid solutions, which corresponds to Sr_2SiO_4. Consequently, our analysis will be confined to the composition of $Na_2Sr_{1-x}Mg_xSi_2O_6:Pr^{3+}$ and $Na_2Sr_{1-x}Ca_xSi_2O_6:Pr^{3+}$ within the range of $x = 0$ to 0.2. The emission spectra of $Na_2MgSi_2O_6:Pr^{3+}$, $Na_2CaSi_2O_6:Pr^{3+}$, and $Na_2BaSi_2O_6:Pr^{3+}$ under UV excitation are shown in Fig. S10. All three phosphors demonstrate ultraviolet luminescence with the maxima moving from about 270 (for Mg composition) to 295 nm (Ba). The red luminescence appears within the 580–680 nm range. Despite a slight alteration in the emission wavelengths within the UV part, the spectra strongly corroborate that the cyclosilicate $Na_2MSi_2O_6$ (where M represents an alkaline earth metal) is a good host for Pr^{3+} to generate emissions in the UVC–UVB and red spectral regions. The possibility to control of the Pr^{3+} UVC and UVB emissions ratio is rarely documented.

Fig. 4a shows the emission spectra of $Na_2Sr_{1-x}Mg_xSi_2O_6:Pr^{3+}$ phosphors upon excitation with 245 nm light. Incorporation of Mg in place of Sr, adversely impacts the emission efficiency of the Pr^{3+}, especially its 5d $\rightarrow$ 4f luminescence in UV. The reduction in red emission intensity occurs at a slow pace. Fig. 4b shows the results of analogous measurements of $Na_2Sr_{1-x}Ca_xSi_2O_6:Pr^{3+}$. The alterations in the lattice dimensions of the solid solution are illustrated in Fig. S8b, c and S9b, c. In comparison to strontium, the ionic radii of magnesium and calcium are comparatively smaller, resulting in lattice contraction upon substitution, which subsequently leads to a reduction in luminescent efficiency.

Also, in this composition, the UVC and UVB bands diminish in intensity with Ca addition. The red light seems slightly less intense when x increases. The integration of the emission spectra for UVC, UVB, and red light results in the overall emission intensities of the three bands (given in Fig. 4c–f). The reduction in luminescence observed in the material following the alloying with Mg^{2+} or Ca^{2+} indicates that the resultant changes in crystal structure reduce the activation energies (ΔE) of 5d $\rightarrow$ 4f luminescence in both materials. Furthermore, the UVB emission associated with Ca or Mg modification does not present any distinct behaviors and generally shows the declining trend seen in UVC emissions. The comparative ratios of overall emission intensities of UVC-to-red light and UVC-to-UVB are illustrated in Fig. 4e and f for Mg- and Ca-co-doped materials, respectively. In general, the observed dependences for Mg and Ca co-dopants are similar, though a more potent decrease of both ratios is seen for the Mg-containing phosphors. The continuous decline in the ratio of the total emission intensities of UVC to red light (Fig. 4e and f) distinctly indicates an increase in the proportion of red light within the

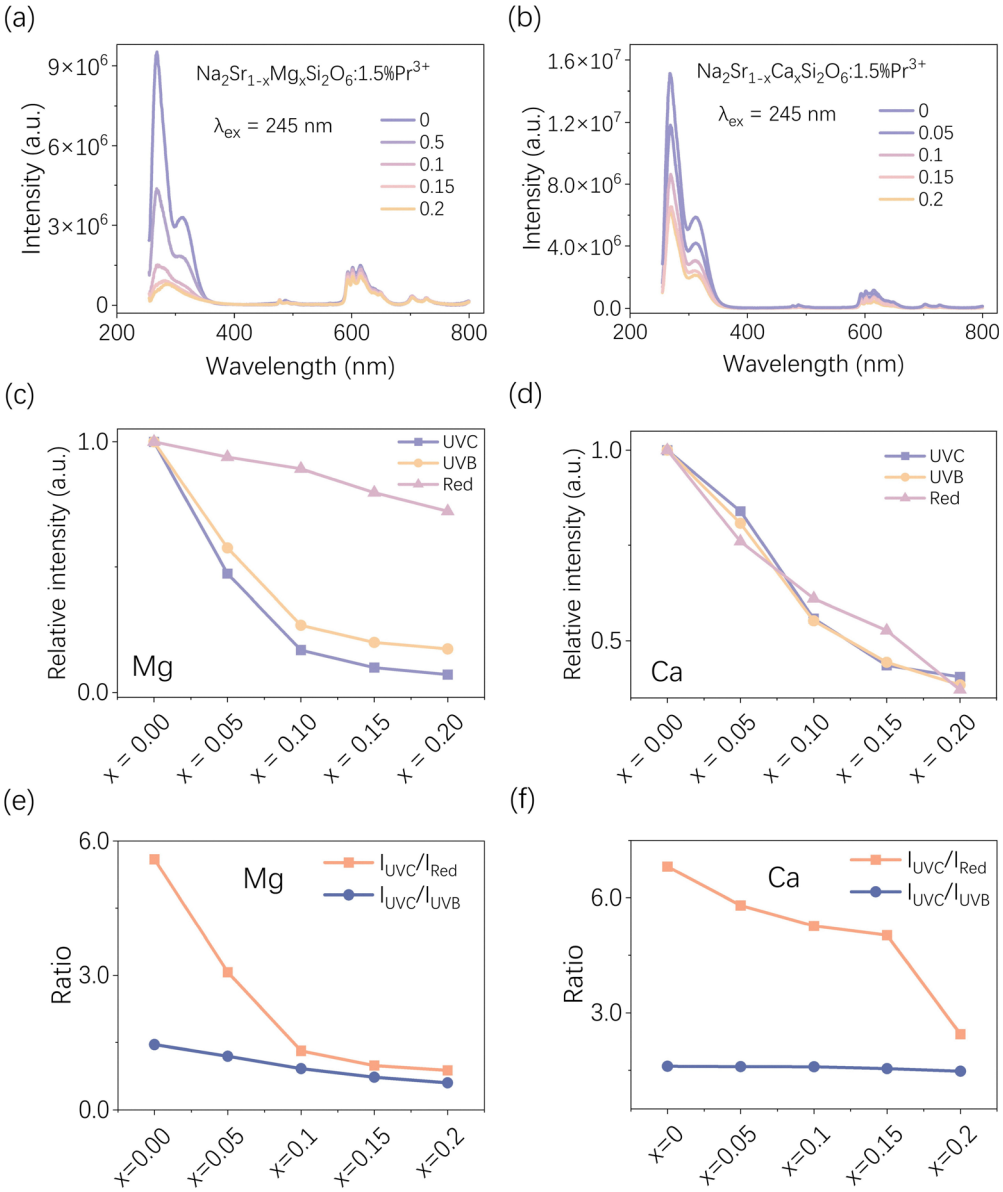

Fig. 4 Emission spectra of (a) $Na_2Sr_{1-x}Mg_xSi_2O_6$:1.5%Pr^{3+}, and (b) $Na_2Sr_{1-x}Ca_xSi_2O_6$:1.5%Pr^{3+} phosphors (x = 0, 0.05, 0.1, 0.15, 0.2) under 245 nm excitation; comparison of the triple-band intensity including the UVC, UVB, and red light regions for (c) $Na_2Sr_{1-x}Mg_xSi_2O_6$:1.5%Pr^{3+}, and (d) $Na_2Sr_{1-x}Ca_xSi_2O_6$:1.5%Pr^{3+} phosphors as a function of x; the ratio of total emission intensity in the UVC region to that in the red wavelength region for (e) $Na_2Sr_{1-x}Mg_xSi_2O_6$:1.5%Pr^{3+}, and (f) $Na_2Sr_{1-x}Ca_xSi_2O_6$:1.5%Pr^{3+} phosphors as a function of x.

total emission, which is consistent with the initial design for regulation.

Subsequently, Ba^{2+} cations, characterized by a greater ionic radius compared to Sr^{2+}, were employed to modify the host lattice composition. From the XRD pattern of $Na_2Sr_{1-x}Ba_xSi_2O_6$:Pr^{3+} (Fig. S11a), it can be observed that a small amount of an impurity phase comes into view when x = 0.35. Therefore, we will only discuss the composition range of $Na_2Sr_{1-x}Ba_xSi_2O_6$:Pr^{3+} for $0 < x < 0.35$.

Contrary to the case of Mg and Ca addition, the emission spectra of $Na_2Sr_{1-x}Ba_xSi_2O_6$:Pr^{3+} under 245 nm excitation (shown in Fig. 5a), present a significant increase of luminescent intensity when Ba^{2+} enters the host. This trend is observed for all three bands (Fig. 5b) up to x = 0.15. The overall enhancement in luminescence intensity is attributed to the local expansion of the crystal structure. The corresponding enlarged regions in Fig. S11b and c (from $2\theta = 32.5^\circ$ to 34° and from 25.6° to 26.7°) reveal continuous lattice changes due to compositional variations between the standard reference ends. As the x content increases, all diffraction peaks gradually shift towards smaller angles, resulting from the substitution of Ba^{2+} ions (1.35 Å, CN = 6) for Sr^{2+} ions (1.18 Å, CN = 6), which leads to lattice expansion. The lattice expansion increases the distance between the ligands and the central ions (such as Pr^{3+}), thereby reducing the crystal field strength. Under the influence of a weaker field, the energy level splitting of Pr^{3+} ions diminishes,

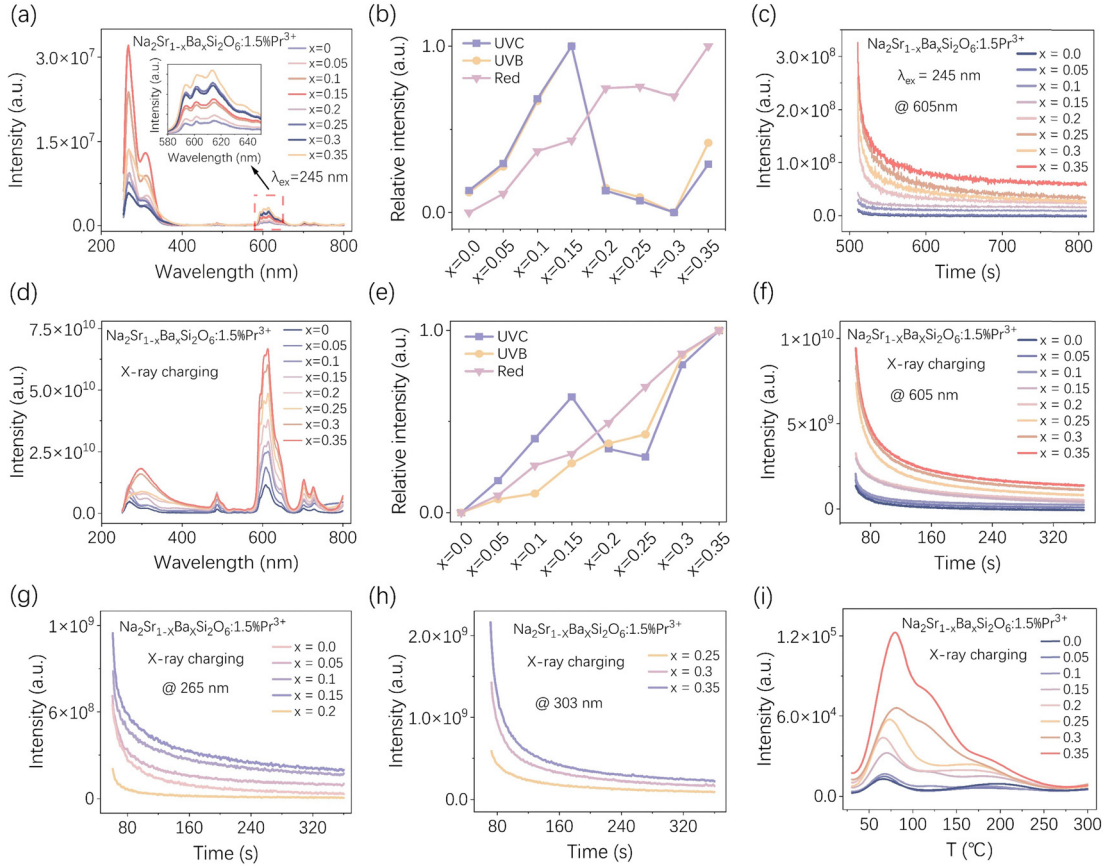

Fig. 5 (a) Emission spectra of $Na_2Sr_{1-x}Ba_xSi_2O_6$:1.5%Pr^{3+} phosphors (x = 0, 0.05, 0.1, 0.15, 0.2, 0.25, 0.3, 0.35) under 245 nm excitation, with an inset showing an enlarged view of the emission spectrum in the 580 nm to 650 nm range. (b) Comparison of emission intensity illustrating the growing trends of UVC, UVB, and red radioluminescent emissions with x for $Na_2Sr_{1-x}Ba_xSi_2O_6$:1.5%Pr^{3+} phosphors. (c) The persistent luminescence decay curve of the $Na_2Sr_{1-x}Ba_xSi_2O_6$:1.5%Pr^{3+} phosphors (x = 0, 0.05, 0.1, 0.15, 0.2, 0.25, 0.3, 0.35) monitored at 605 nm after 245 nm irradiation. (d) Radioluminescence spectra of $Na_2Sr_{1-x}Ba_xSi_2O_6$:1.5%Pr^{3+} phosphors (x = 0, 0.05, 0.1, 0.15, 0.2, 0.25, 0.3, 0.35) under X-ray excitation. (e) A radioluminescence intensity comparison showing the trend of total emission intensity in the UVC, UVB, and red light regions with increasing x for $Na_2Sr_{1-x}Ba_xSi_2O_6$:1.5%Pr^{3+} phosphors. The persistent luminescence decay curve of $Na_2Sr_{1-x}Ba_xSi_2O_6$:1.5%Pr^{3+} phosphors monitored (f) at 608 nm, (g) at 265 nm, and (h) at 303 nm, after irradiation with X-rays. (i) Thermoluminescence (TL) glow curves of $Na_2Sr_{1-x}Ba_xSi_2O_6$:1.5%Pr^{3+} phosphors (x = 0, 0.05, 0.1, 0.15, 0.2, 0.25, 0.3, 0.35) after exposure to X-rays.

potentially relaxing the selection rules for electronic transition processes, thus increasing the probability of radiative transitions. Additionally, the weak crystal field facilitates forbidden transitions, which can enhance the efficiency of f–d transitions. Moreover, the substitution of Sr^{2+} with Ba^{2+} can alter the symmetry of the local structure; since the transitions of rare earth ions are highly sensitive to local symmetry, these changes may directly affect the selection rules for Pr^{3+}, increasing the probability of radiative transitions and improving luminescence efficiency.

A higher content of Ba also reduces the overall emission. For example, up to x = 0.15, the effective enlargement of the site where Pr^{3+} goes with increasing Ba content seems to increase the activation energy of the Pr^{3+} 5d → 4f luminescence quenching. This might result from lower crystal field splitting of the 5d orbitals due to some elongation of the Pr^{3+}–O^{2-} distances. Furthermore, the progressively enhanced ratio of UVC to red emission intensities (refer to Fig. S12) further reveals the viability of augmenting UVC radiation transition probabilities by elevating ΔE. When Ba^{2+} substitutes for Sr^{2+}, the introduction of a larger ion leads to distortion and expansion of the crystal structure, affecting the coordination environment and the relative arrangement of atoms. This results in a reduction of the splitting of the Pr^{3+} 4f5d energy levels, indicating that the interactions driven by the surrounding environment become weaker. This decreased splitting increases the energy difference ΔE between the 4f5d state and the next lower ^3P_J energy level, thereby enhancing the UVC luminescence. A higher content of Ba reduces the overall emission quickly. When the Ba^{2+} content increases to above x = 1.5, a significant decrease in UVC luminescence intensity occurs.

Fig. 5c presents the persistent luminescence decay curve of the $Na_2Sr_{1-x}Ba_xSi_2O_6$:1.5%Pr^{3+} phosphors (x = 0, 0.05, 0.1, 0.15, 0.2, 0.25, 0.3, 0.35) monitored at 605 nm after 245 nm irradiation. The afterglow intensity exhibits a gradual enhancement with the increasing value of x, especially above x = 0.15. This is true for all observed emissions, UVC, UVB, and the red one.

Fig. 5d presents the radioluminescence spectra of $Na_2Sr_{1-x}Ba_xSi_2O_6:Pr^{3+}$. As the content of Ba^{2+} cations increases, the $Na_2Sr_{1-x}Ba_xSi_2O_6:Pr^{3+}$ phosphors exhibit a progressive transition from emitting UVC radiation to generating UVB radiation. When the value of x exceeds 0.25, the radioluminescence exhibits a pronounced broad maximum at 300 nm, which is around the long-wavelength peak of the 5d → 4f luminescence of Pr^{3+} when the host contains less Ba. Clearly, the significant decrease in UVC luminescence intensity observed for $x > 1.5$ during UV excitation is attributed to the transition from UVC to UVB luminescence.

Analysis of the trends in the radioluminescent emission band intensities with changing x (Fig. 5e) indicates that with an increase of Ba^{2+} concentration the UVC band grows in intensity up to $x = 0.15$ and then diminishes for yet higher x values by about 50% to finally grow again. On the contrary, UVB and red emissions grow quite systematically with increasing x. Since the shape of the luminescence in the range of 5d → 4f emission clearly changes with increasing x, getting systematically broader and losing the characteristic doublet structure, we may assume that Pr^{3+} occupies a number of distorted symmetry sites – the effect of distortions resulting from Ba entering the host lattice.

Fig. 5f–h illustrate the persistent luminescence decay profiles of $Na_2Sr_{1-x}Ba_xSi_2O_6:Pr^{3+}$ across the UVC, UVB, and the red band following the X-ray exposure. The phosphors demonstrate commendable afterglow characteristics across all three wavelength domains. Yet, while the red persistent luminescence grows systematically from $x = 0$ to $x = 0.35$ the UVC persistent emission grows up to $x = 0.15$ to decrease for higher x. The UVB afterglow is most significant for the highest $x = 0.35$. The different dependence of UVC and UVB persistent luminescence on x has a clear connection with the already discussed (see Fig. 5d) changes in spectral distribution of the emission in UV upon X-rays. The TL glow curves of $Na_2Sr_{1-x}Ba_xSi_2O_6:Pr^{3+}$ phosphors after X-ray irradiation (Fig. 5i) show a potent increase in charge carriers trapping centers with increasing Ba content. Initially, up to $x = 0.1$, the TL glow curve of the solid solution shows minimal variations and low intensity of both observed TL peaks, at about 65 °C and ~200 °C. However, when x reaches and exceeds the value of 0.15, the TL peaks broaden, their intensities quickly grow, and a new intense component

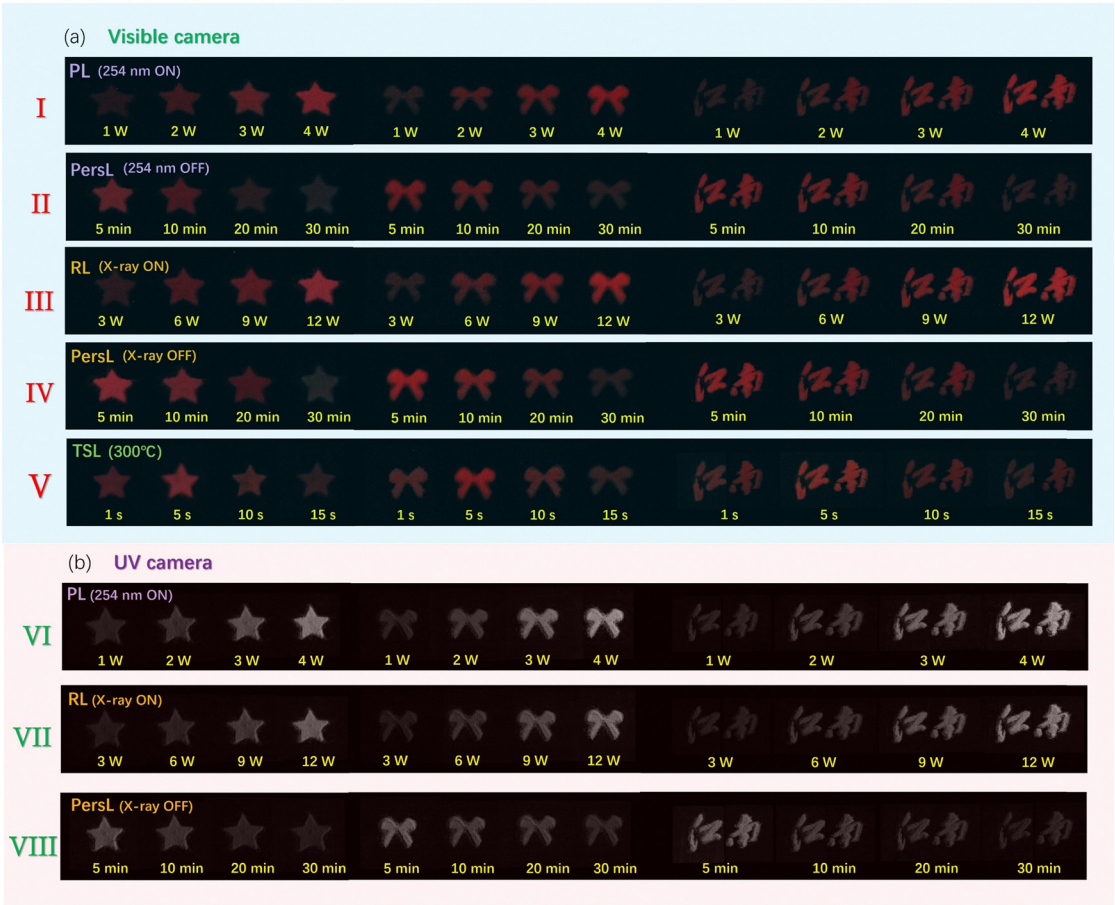

Fig. 6 (a) Images of red photoluminescence (I, 254 nm), red persistent luminescence (II, after 254 nm), red radioluminescence (III, X-ray), red persistent luminescence (IV, after X-rays) and red thermally stimulated luminescence (V) from patterns of star, bow knot, and Chinese characters for $Na_2Sr_{0.85}Ba_{0.15}Si_2O_6$:1.5%$Pr^{3+}$ phosphors under 254 nm or X-ray irradiation (captured with a standard visible light camera). (b) Images of UV photoluminescence (VI, 254 nm), UV radioluminescence (VII, X-ray) and UV persistent luminescence (VIII, after X-ray) of stars, bows, and Chinese characters for $Na_2Sr_{0.85}Ba_{0.15}Si_2O_6$:1.5%$Pr^{3+}$ phosphors under 254 nm or X-ray irradiation (captured with a UV sensitive camera).

peaking at about 120 °C develops. Consequently, beyond x = 0.25, the firstly separated TL peaks widen so severely that they overlap forming a broad slightly structured TL band with maximum around 75 °C and covering the range of 30–250 °C. These data prove a progressively and quickly growing population of trapped charge carriers and quite significant reconstruction of the carriers trapping sites leading to a growth of their population and changes of their depths with x increasing from 0.1 to 0.35. TL fading was also performed in $Na_2Sr_{1-x}Ba_xSi_2O_6:Pr^{3+}$ phosphors after X-ray irradiation (as displayed in Fig. S13 and S14). TL glow curves were recorded with different delay time after irradiation. The liberation of charge carriers comes from both shallow traps (below 100 °C) and deeper traps (100–300 °C). The detrapping from shallow traps is predominantly thermally activated. Conversely, the liberation from deep traps can be attributed to both thermally activated processes and quantum tunneling. Consequently, both shallow and deep traps contribute to UV persistent luminescence.

Fig. 6 presents the luminescent patterns of a star, a bow knot, and Chinese characters made from $Na_2Sr_{0.85}Ba_{0.15}Si_2O_6$: 1.5%$Pr^{3+}$ under varying excitation sources and bright-dark conditions. Utilizing a standard visible-sensitive imaging system (Fig. 6a), it is evident that in a low-light setting, the luminance of the captured image progressively intensifies when illuminated by a 254 nm light source at varying power levels. The images are visible by the naked eye for 30 minutes, even in the absence of the illumination source. Upon high-energy X-ray irradiation, the intensity of the luminescent and afterglow image is significantly augmented. Furthermore, after irradiation the specimen with X-rays and letting it to terminate afterglow at room temperature afterwards, and subjecting it to a thermal treatment at 300 °C can induce a significant red thermally stimulated luminescence. All these images of red photoluminescence, red persistent luminescence, red radioluminescence and red thermally stimulated luminescence can be clearly seen from patterns of star, bow knot, and Chinese characters, confirming the co-existence of multi-mode visible luminescence. Moreover, the utilization of a UV-sensitive imaging system (Fig. 6b) facilitates the precise identification of UVC and UVB emissions under 254 nm or X-ray irradiations with different powers, even in high intensity ambient light conditions (bright daylight environments). The afterglow emission of UVC–UVB following X-ray irradiation can be continuously assessed by monitoring variations in the luminescence of the pattern. Consequently, the viability and demonstration of UVC–UVB and red light imaging have been substantiated under both bright-field and dark-field conditions, indicating the significant potential of the phosphor for important practical applications.

The emission spectra of the majority of persistent luminescent materials are predominantly confined to the visible and near-infrared wavelengths, necessitating the observation of emission signals in dark conditions to avoid an interference from ambient daylight. In contrast, $Na_2Sr_{0.85}Ba_{0.15}Si_2O_6$: 1.5%$Pr^{3+}$ demonstrates significant potential for high-contrast daylight-blind detection or imaging in both bright indoor and outdoor environments, owing to its UVC–UVB persistent luminescence that produce minimal background interference (since solar UVC radiation is absent at the Earth's surface). Furthermore, the synergistic effect of UVC–UVB and visible radiation in triple luminescence allows considering applications for the phosphor in anti-counterfeiting measures and data encryption technologies.

3. Conclusion

We have developed a series of Pr^{3+}-doped cyclosilicate-based UVC–UVB-red triple-band persistent phosphor ($Na_2SrSi_2O_6:Pr^{3+}$) for the first time. This phosphor exhibits intense UVC–UVB and red long afterglow lasting over 30 minutes. Alongside thorough spectral analyses, trapping and detrapping processes have been studied using a set of X-ray charging and thermoluminescence measurements to understand the underlying triple-band luminescence mechanisms. By manipulating the composition *via* the partial substitution of Sr sites with Mg/Ca/Ba ions, triple-band PersL and emission variations were carefully investigated. The incorporation of smaller ionic radius dopants, such as Mg^{2+} or Ca^{2+}, effectively enhances the red emission intensity of the phosphor. In contrast, the introduction of the larger ionic radius dopant Ba^{2+} not only enhances the fraction of UVC emission but also improves the overall luminescent efficacy. Moreover, with the increasing content of Ba^{2+}, the phosphor accomplishes a luminescence evolution from UVC to UVB within the deep ultraviolet spectrum, thereby adjusting the probabilities of the two radiative transitions. Notably, the applications of this phosphor were assessed in bright-field and dark-field imaging, showcasing its considerable potential for high-contrast monitoring in bright daylight, anti-counterfeiting applications, and advanced optical marking technologies. This work advances the development of persistent luminescence materials presenting combined visible and invisible emissions and appears a good example of engineering the cyclosilicate matrices for luminescence managing.

4. Experimental section

4.1. Materials preparation

The phosphor with the composition $Na_2SrSi_2O_6:Pr^{3+}$ was synthesized using conventional high-temperature solid-state reactions. The raw materials of Na_2CO_3 (99.99%, Aladdin), Sr_2CO_3 (99.99%, Aladdin), SiO_2 (99.99%, Aladdin), and Pr_2O_3 (99.99%, Aladdin) were weighed according to their stoichiometric ratios. These materials were mixed in an agate mortar for 30 minutes and then pressed into discs 13 mm in diameter using a 15-ton dry pressing machine. The formed samples were heated in a tube furnace (KTL1700-80, Nanjing Laibu Tech) at 1000 °C for 4 hours, with a heating rate of 300 °C per hour. After heating, the samples were allowed to cool naturally to room temperature overnight. Finally, the cooled samples were ground again to obtain a homogeneous powder for further analysis. $Na_2Sr_{1-x}Mg_xSi_2O_6:Pr^{3+}$ (x = 0.05, 0.1, 0.15, 0.2, 0.25), $Na_2Sr_{1-x}Ca_xSi_2O_6:Pr^{3+}$ (x = 0.05, 0.1, 0.15, 0.2, 0.25) and $Na_2Sr_{1-x}Ba_xSi_2O_6:Pr^{3+}$

(x = 0.05, 0.1, 0.15, 0.2, 0.25, 0.3, 0.35) were prepared in the same manner.

4.2. Structural characterization

The phases and purity of the samples were analyzed using an X-ray diffractometer (D8 ADVANCE, Bruker, Germany) with Cu Kα1 radiation (1.5406 Å) at a tube voltage of 40 kV and a current of 40 mA. Scanning was conducted at a speed of 2.4° per minute within a 2θ range of 10° to 80°. The resulting XRD patterns were compared against standard reference patterns for $Na_2SrSi_2O_6$ (PDF no. 01-074-3938). Scanning electron microscopy (SEM) images were obtained using an FEI Quanta 650 FEG. Electron paramagnetic resonance (EPR) spectra were collected with a Bruker ESR 5000 spectrometer (X-band at about 9.6 GHz). An X-ray photoelectron spectrometer (AXIS Supra by Kratos Analytical Inc., using monochromatized Al Kα radiation ($h\nu$ = 1486.6 eV, 150 W) as X-ray source with a base pressure of 10^{-9} torr) was applied to collect the XPS spectra.

4.3. Photoluminescence and photoluminescence excitation characterization

A high-resolution spectrofluorometer (FS5, Edinburgh Instruments, UK) with a monochromated 450 W Xenon lamp was utilized to measure the photoluminescence (PL), photoluminescence excitation (PLE), and 2D PL-PLE spectra at room temperature. All spectra were automatically adjusted for detector response (PL) and incident radiation intensity (PLE).

4.4. Persistent luminescence decay characterization and thermoluminescence characterization

The measurement of X-ray excited luminescence and persistent luminescence decay curves was conducted using a spectrofluorometer (FLS1000, Edinburgh Instruments, UK) fitted with an X-ray tube (the anode type is tungsten, with an adjustable voltage of 4 to 70 kV and a maximum power of 12 W, TUB00154-SA-W06, MOXTEK Inc., USA). Before each decay experiment, the samples were allowed to stabilize in the testing environment for a few minutes until the emission intensity returned to background levels, ensuring accurate comparisons. The thermoluminescence experiments were conducted using a custom-made measurement system, which included a dark chamber, various light sources (software-controlled X-ray tube and 254 nm UV lamps with a power of 1 W, 2 W, 3 W, or 4 W), a TL heating platform (SL08, Rongfan Technology, China), and a R928 photomultiplier tube (Hamamatsu Photonics, Japan). During the TL measurement, a constant heating rate of $\beta = 1\ ^\circ C\ s^{-1}$ was employed. A thermal cleaning was performed before each experimental cycle to empty carriers from all related traps. Photographs of the samples were captured using a visible-light-sensitive camera (Canon T5i), while UVC–UVB luminescence images were recorded with a UV CCD camera (ARTCAM-UV, ARTRAY CO., LTD, China). This UV-sensitive CCD camera effectively captures UVC–UVB luminescence in the range of 230–320 nm, displaying UVC–UVB radiation as a white image, with brightness proportional to the emission intensity.

Conflicts of interest

There are no conflicts to declare.

Data availability

The data supporting this article and all supporting figures have been included as part of the SI. See DOI: **https://doi.org/10.1039/d5mh01199j**

Acknowledgements

The authors acknowledge the financial support from the National Natural Science Foundation of China (No. 12204197). EZ acknowledges support from the Polish National Science Centre (NCN) under grant UMO-2024/53/B/ST5/02551.

References

1 D. Van der Heggen, J. J. Joos, A. Feng, V. Fritz, T. Delgado, N. Gartmann, B. Walfort, D. Rytz, H. Hagemann, D. Poelman, B. Viana and P. F. Smet, Persistent luminescence in strontium aluminate: A roadmap to a brighter future, *Adv. Funct. Mater.*, 2022, **32**, 2208809.
2 Y. Zhuang, L. Wang, Y. Lv, T.-L. Zhou and R.-J. Xie, Optical data storage and multicolor emission readout on flexible films using deep-trap persistent luminescence materials, *Adv. Funct. Mater.*, 2018, **28**, 1705769.
3 D. Poelman, D. Van der Heggen, J. Du, E. Cosaert and P. F. Smet, Persistent phosphors for the future: Fit for the right application, *J. Appl. Phys.*, 2020, **128**, 240903.
4 X. Zhang, H. Suo, Y. Wang, B. Chen, W. Zheng, Q. Wang, Y. Wang, Z. Zeng, S.-W. Tsang, D. Tu and F. Wang, Systematic tuning of persistent luminescence in a quaternary wurtzite crystal through synergistic defect engineering, *Laser Photonics Rev.*, 2023, **17**, 2300132.
5 J. Du, X. Wang, S. Sun, Y. Wu, K. Jiang, S. Li and H. Lin, Pushing Trap-Controlled Persistent Luminescence Materials toward Multi-Responsive Smart Platforms: Recent Advances, Mechanism, and Frontier Applications, *Adv. Mater.*, 2024, **36**, 2314083.
6 S. Lin, H. Lin, Q. Huang, Y. Cheng, J. Xu, J. Wang, X. Xiang, C. Wang, L. Zhang and Y. Wang, A photostimulated $BaSi_2O_5$:Eu^{2+},Nd^{3+} phosphor-in-glass for erasable-rewritable optical storage medium, *Laser Photonics Rev.*, 2019, **13**, 1900006.
7 X. Zhou, L. Ning, J. Qiao, Y. Zhao, P. Xiong and Z. Xia, Interplay of defect levels and rare earth emission centers in multimode luminescent phosphors, *Nat. Commun.*, 2022, **13**, 7589.
8 D. Kulesza, A. J. J. Bos and E. Zych, The effect of temperature and excitation energy of the high- and low-spin 4f → 5d transitions on charging of traps in Lu_2O_3:Tb,M (M = Ti, Hf), *Acta Mater.*, 2022, **231**, 117852.
9 P. Wang, J. Du, T. Wang, S. Lyu, R. Van Deun, D. Poelman and H. Lin, Visualizing temperature inhomogeneity using

thermo-responsive smart materials, *Mater. Horiz.*, 2023, **10**, 5684–5693.
10 Q. Zhang, Z. Yang, X. Zhou, M. Delaey, M. Wang, R. Fu, S. Lei, H. Vrielinck and D. Poelman, Achieving High Quantum Efficiency in Mn^{5+} Activated Phosphors for NIR-II Deep Bioimaging Application, *Laser Photonics Rev.*, 2024, **18**, 2400781.
11 H. Suo, N. Wang, Y. Zhang, X. Zhang, J. Xiang, X. Wang, G. Xing, D. Guo, J. Chang, Y. Wang, P. Li, Z. Wang, Y. Zhang, B. Chen, S. Li, C. Guo and F. Wang, Excitation-mode-selective emission through multiexcitonic states in a double perovskite single crystal, *Light: Sci. Appl.*, 2025, **14**, 21.
12 L. Wang, D. Tu, C. Li, S. Han, F. Wen, S. Yu, X. Yi, Z. Xie and X. Chen, Engineering trap distribution to achieve multicolor persistent and photostimulated luminescence from ultraviolet to near-infrared II, *Matter*, 2023, **6**, 4261–4273.
13 J. Du and D. Poelman, Identifying Near-Infrared Persistent Luminescence in Cr^{3+}-Doped Magnesium Gallogermanates Featuring Afterglow Emission at Extremely Low Temperature, *Adv. Opt. Mater.*, 2020, **8**, 1901848.
14 H. Shi and Z. An, Ultraviolet afterglow, *Nat. Photonics*, 2019, **13**, 74–75.
15 Y.-M. Yang, Z.-Y. Li, J.-Y. Zhang, Y. Lu, S.-Q. Guo, Q. Zhao, X. Wang, Z.-J. Yong, H. Li, J.-P. Ma, Y. Kuroiwa, C. Moriyoshi, L.-L. Hu, L.-Y. Zhang, L.-R. Zheng and H.-T. Sun, X-ray-activated long persistent phosphors featuring strong UVC afterglow emissions, *Light: Sci. Appl.*, 2018, **7**, 88.
16 X. Wang and Y. Mao, Emerging Ultraviolet Persistent Luminescent Materials, *Adv. Opt. Mater.*, 2022, **10**, 2201466.
17 X. Zhou, J. Qiao, Y. Zhao, K. Han and Z. Xia, Multi-responsive deep-ultraviolet emission in praseodymium-doped phosphors for microbial sterilization, *Sci. China Mater.*, 2022, **65**, 1103–1111.
18 X. Wang, Y. Chen, F. Liu and Z. Pan, Solar-blind ultraviolet-C persistent luminescence phosphors, *Nat. Commun.*, 2020, **11**, 2040.
19 H. Li, Y. Yang, P. Li, D. Peng and L. Li, Force-Induced Ultraviolet C Luminescence of Pr^{3+}-Doped $Sr_2P_2O_7$ for X-Ray Dosimetry, *Adv. Mater.*, 2024, **36**, 2411804.
20 B. Yang, Z. Yu, X. Liu, Y. Liu, F. Liu, H. Wu, J. Zhang, X.-J. Wang and Y. Liu, Photostimulated Ultraviolet Luminescence for Anti-Counterfeiting in Daylight Conditions, *Laser Photonics Rev.*, 2025, **19**, 2401606.
21 X. Zhao, F. Liu, Z. Yu, X. Li, C. Wang, F. Chen and X.-J. Wang, Sunlight stimulated solar-blind ultraviolet phosphor, *Phys. Rev. Res.*, 2022, **4**, L012028.
22 X. Lv, Y. Liang, Y. Zhang, D. Chen, X. Shan and X.-J. Wang, Deep-trap ultraviolet persistent phosphor for advanced optical storage application in bright environments, *Light: Sci. Appl.*, 2024, **13**, 253.
23 W. Zhao, L. Li, T. Li, J. Qiu and Y. Yang, UVB Persistent Luminescence of CaF_2:Gd^{3+} for Radiation Labeling and Tracing, *Adv. Opt. Mater.*, 2024, **12**, 2401320.
24 P. Lv, L. Li, C. Wang, Z. Wu, J. Qiu and Y. Yang, 450 nm Photon-Pumped Ultraviolet-C Luminescence for Multifunctional Applications, *Laser Photonics Rev.*, 2022, **16**, 2200389.
25 Y. Wang, P. Zhou, H. Lin and J. Du, Optically driven ultraviolet-C glowing from an in situ trapping–detrapping approach, *Opt. Lett.*, 2024, **49**, 5623–5626.
26 L. Zi, L. Li, C. Wang, F. Yang, S. Feng, P. Lv and Y. Yang, Triple-Responsive Visible-To-Ultraviolet-C Upconverted Photons for Multifunctional Applications, *Adv. Opt. Mater.*, 2024, **12**, 2301881.
27 S. K. Sharma, J. James, S. K. Gupta and S. Hussain, UV-A,B,C Emitting Persistent Luminescent Materials, *Materials*, 2023, **16**, 236.
28 X. Wang and Y. Mao, Achieving Ultraviolet C and Ultraviolet B Dual-Band Persistent Luminescence by Manipulating the Garnet Structure, *Adv. Opt. Mater.*, 2022, **10**, 2102157.
29 E. L. Cates, A. P. Wilkinson and J.-H. Kim, Visible-to-UVC upconversion efficiency and mechanisms of $Lu_7O_6F_9$:Pr^{3+} and Y_2SiO_5:Pr^{3+} ceramics, *J. Lumin.*, 2015, **160**, 202–209.
30 C. Wang, M. Deng, Y. Tang, T. Sun, M. Wang, J. Wang, Z. Zhou and J. Wang, Crystal Field Engineering of Pr-Activated Gehlenite with Near Golden Ultraviolet C Emission for 100% Sterilization Efficiency, *J. Phys. Chem. Lett.*, 2023, **14**, 6386–6394.
31 A. Antuzevics, G. Krieke, G. Doke, P. Rodionovs, D. Nilova, J. Cirulis, A. Fedotovs and U. Rogulis, Role of Paramagnetic Aluminum Hole Centers in UV–C Persistent Luminescence of $Ca_2Al_2SiO_7$:Pr^{3+}, *J. Phys. Chem. C*, 2024, **128**, 21846–21854.
32 A. M. Srivastava, Aspects of Pr^{3+} luminescence in solids, *J. Lumin.*, 2016, **169**, 445–449.
33 A. Zych, M. de Lange, C. de Mello Donegá and A. Meijerink, Analysis of the radiative lifetime of Pr^{3+} d–f emission, *J. Appl. Phys.*, 2012, **112**, 013536.
34 E. L. Cates, A. P. Wilkinson and J.-H. Kim, Delineating Mechanisms of Upconversion Enhancement by Li^+ Codoping in Y_2SiO_5:Pr^{3+}, *J. Phys. Chem. C*, 2012, **116**, 12772–12778.
35 P. Lv, L. Li, Z. Yin, C. Wang and Y. Yang, Visible-to-ultraviolet-C upconverted photon for multifunction *via* Ca_2SiO_4:Pr^{3+}, *Opt. Lett.*, 2022, **47**, 4435–4438.
36 Y. Zhang, X. Shan, X. Lv, D. Chen, S. Miao, W. Wang and Y. Liang, Multimodal luminescence in Pr^{3+} single-doped Li_2CaSiO_4 phosphor for optical information storage and anti-counterfeiting applications, *Chem. Eng. J.*, 2023, **474**, 145886.
37 G. Malavasi, G. Lusvardi, A. Pedone, M. C. Menziani, M. Dappiaggi, A. Gualtieri and L. Menabue, Crystallization Kinetics of Bioactive Glasses in the ZnO–Na_2O–CaO–SiO_2 System, *J. Phys. Chem. A*, 2007, **111**, 8401–8408.
38 V. Kahlenberg, Preparation and crystal structure of $Na_2SrSi_2O_6$—a cyclosilicate with perovskite-type features, *J. Alloys Compd.*, 2004, **366**, 132–135.
39 J. Li and Y. Wang, Tunable emission with efficient energy transfer in $Na_2SrSi_2O_6$:Ce^{3+},Tb^{3+} phosphor for near-UV LED, *Opt. Mater.*, 2019, **88**, 648–652.
40 Y. Q. Jia, Crystal radii and effective ionic radii of the rare earth ions, *J. Solid State Chem.*, 1991, **95**, 184–187.
41 P. Bolek, T. van Swieten, J. Zeler, A. Meijerink and E. Zych, Luminescence Thermometry of Pr^{3+}-Doped $Sr_3Y_2Ge_3O_{12}$ and $Sr_3Sc_2Ge_3O_{12}$ Submicron Garnets Spanning the 13–1025 K

Range and New Insight to Their Spectroscopy, *Chem. Mater.*, 2024, **36**, 8894–8909.

42 Y. Du, Z. Jin, Z. Li, T. Sun, H. Meng, X. Jiang, Y. Wang, D. Peng, J. Li, A. Wang, H. Zou, F. Rao, F. Wang and X. Chen, Tuning the 5d State of Pr^{3+} in Oxyhalides for Efficient Deep Ultraviolet Upconversion, *Adv. Opt. Mater.*, 2024, **12**, 2400971.

43 X. Wang and Y. Mao, Recent advances in Pr^{3+}-activated persistent phosphors, *J. Mater. Chem. C*, 2022, **10**, 3626–3646.

44 J. Du, A. Feng and D. Poelman, Temperature Dependency of Trap-Controlled Persistent Luminescence, *Laser Photonics Rev.*, 2020, **14**, 2000060.

45 K. Van den Eeckhout, A. J. J. Bos, D. Poelman and P. F. Smet, Revealing trap depth distributions in persistent phosphors, *Phys. Rev. B: Condens. Matter Mater. Phys.*, 2013, **87**, 045126.

46 J. Du, J. Zhang, T. Wang, P. Zhou, L. Cao, Q. Liu and H. Lin, Brighten strontium aluminate long-persistence materials via optimizing defect energy level distribution, *Mater. Today Phys.*, 2023, **38**, 101229.

47 S. Zhang, F. Zhao, S. Liu, Z. Song and Q. Liu, An improved method to evaluate trap depth from thermoluminescence, *J. Rare Earths*, 2025, **43**, 262–269.

48 Y. Song, H. Zhao, Y. Zi, J. Qiu, Z. Song, X. Bai, J. Liao and Z. Yang, X-ray-Irradiation-Induced Discoloration and Persistent Radioluminescence for Reversible Dual-Mode Imaging and Detection Applications, *ACS Energy Lett.*, 2023, **8**, 2232–2240.

49 H. Idriss, On the wrong assignment of the XPS O1s signal at 531–532 eV attributed to oxygen vacancies in photo- and electro-catalysts for water splitting and other materials applications, *Surf. Sci.*, 2021, **712**, 121894.

50 Q.-H. Wu, A. Thißen and W. Jaegermann, XPS and UPS study of Na deposition on thin film V_2O_5, *Appl. Surf. Sci.*, 2005, **252**, 1801–1805.

51 M. Sterrer, E. Fischbach, T. Risse and H.-J. Freund, Geometric Characterization of a Singly Charged Oxygen Vacancy on a Single-Crystalline MgO(001) Film by Electron Paramagnetic Resonance Spectroscopy, *Phys. Rev. Lett.*, 2005, **94**, 186101.